Neurobiology of Disease

Global and Regional Damages in Retinal Ganglion Cell Axon Bundles Monitored Non-Invasively by Visible-Light Optical Coherence Tomography Fibergraphy

Marta Grannonico,[1*] David A. Miller,[2*] Mingna Liu,[1*] Pedro Norat,[1] Christopher D. Deppmann,[1,4] Peter A. Netland,[3] Hao F. Zhang,[2] and Xiaorong Liu[1,3,4,5]

[1]Department of Biology, University of Virginia, Charlottesville, Virginia 22904, [2]Department of Biomedical Engineering, Northwestern University, Evanston, Illinois 60208, [3]Department of Ophthalmology, University of Virginia, Charlottesville, Virginia 22904, [4]Program in Fundamental Neuroscience, University of Virginia, Charlottesville, Virginia 22904, and [5]Department of Psychology, University of Virginia, Charlottesville, Virginia 22904

Retinal ganglion cells (RGCs) exhibit compartmentalized organization, receiving synaptic inputs through their dendrites and transmitting visual information from the retina to the brain through the optic nerve. Little is known about the structure of RGC axon bundles extending from individual RGC somas to the optic nerve head (ONH) and how they respond to disease insults. We recently introduced visible-light optical coherence tomography fibergraphy (vis-OCTF), a technique for directly visualizing and analyzing mouse RGC axon bundles *in vivo*. In this study, we validated vis-OCTF's ability to quantify RGC axon bundles with an increased number of RGCs using mice deficient in BCL2-associated X protein ($BAX^{-/-}$). Next, we performed optic nerve crush (ONC) injury on wild-type (WT) mice and showed that the changes in RGC axon bundle width and thickness were location-dependent. Our work demonstrates the potential of vis-OCTF to longitudinally quantify and track RGC damage at single axon bundle level in optic neuropathies.

Key words: **axon bundles; *in vivo* imaging; optic neuropathy; retinal ganglion cell; vis-OCT fibergram; visible light optical coherence tomography**

Significance Statement

Nearly all clinical and preclinical studies measure the retinal nerve fiber (RNFL) thickness as the sole indicator of retinal ganglion cell (RGC) damage without investigating RGC axon bundles directly. We demonstrated visible-light optical coherence tomography fibergraphy (vis-OCTF) to directly quantify global and regional RGC axon bundle organizations *in vivo* as a new biomarker for RGC health. We validated *in vivo* vis-OCTF measures using both confocal microscopy of the immunostained flat-mounted retina and numerical simulations. Vis-OCTF for monitoring RGC axon bundle organization has the potential to bring new insight into RGC damage in optic neuropathies.

Introduction

Retinal ganglion cells (RGCs) are highly specialized cells with subcompartments, each with unique functions (Sernagor et al., 2001; Donato et al., 2019). RGCs receive synaptic inputs through their dendritic trees in the inner plexiform layer (IPL) and send the output to the brain via their axons (Sernagor et al., 2001; Cang et al., 2018). Under disease conditions, RGCs have distinct self-destructive programs that are also spatially compartmentalized (Whitmore et al., 2005; Syc-Mazurek and Libby, 2019). Extensive studies have focused on the degeneration of RGC dendrites and soma and regeneration of RGC axonal projections to the brain (Feng et al., 2013; Chen et al., 2015a; Della Santina and Ou, 2017; Tran et al., 2019). Yet, the part of the RGC axon extending from the RGC soma toward the optic nerve head (ONH) in the retinal nerve fiber layer (RNFL) had been understudied. Little is known whether and how these axon bundles degenerate in response to disease insult. Because the RGC axon

Received Apr. 19, 2021; revised Aug. 18, 2021; accepted Oct. 15, 2021.

Author contributions: X.L., M.G., D.A.M., M.L., and H.F.Z. designed research; X.L., M.G., D.A.M., M.L., P.N., and H.F.Z. performed research; X.L., C.D.D., and H.F.Z. contributed unpublished reagents/analytic tools; X.L., M.G., D.A.M., M.L., P.N., P.A.N., and H.F.Z. analyzed data; X.L., M.G., and D.A.M. wrote the first draft of the paper; X.L., M.G., D.A.M., M.L., P.N., C.D.D., P.A.N., and H.F.Z. edited the paper; X.L., M.G., D.A.M., and H.F.Z. wrote the paper.

This work was supported in part by National Institutes of Health Grants R01EY026078, R01EY029121, R01EY028304, R01EY019949, R01EY026286, and R44EY026466. We thank Ashley Mason for her help with BAX mice breeding. We also thank Jingyi Gao, James Cole, and Prof. Ignacio Provencio for their fruitful discussions.

*M.G., D.A.M., and M.L. contributed equally to this work.

H.F.Z. has financial interests in Opticent Health, which did not support this work. All other authors declare no competing financial interests.

Correspondence should be addressed to Hao F. Zhang at hfzhang@northwestern.edu or Xiaorong Liu at xl8n@virginia.edu.

https://doi.org/10.1523/JNEUROSCI.0844-21.2021

bundles are located in the RNFL along the inner surface of the retina, which makes them easily accessible to noninvasive retinal imaging, we explored whether we could characterize the RGC axon bundle morphology *in vivo* as a new indicator for RGC health.

Optic nerve damage induced by trauma or diseases, such as glaucoma or optic neuritis, causes RGC loss leading to often irreversible vision loss (Quigley, 2011; Jonas et al., 2017). Different techniques, including optical coherence tomography (OCT; Dong et al., 2017; Hood, 2017), confocal scanning laser ophthalmoscopy (cSLO; Wollstein et al., 1998, 2000), and scanning laser polarimetry (Anton et al., 1997; Da Pozzo et al., 2009), are applied to detect the morphologic changes associated with RGC damage, such as neuroretinal rim and RNFL thinning. However, RNFL thickness measurements can be inconsistent because of variations in axial resolution (from 5 to 10 μm) and segmentation algorithms used across various imaging platforms (Dong et al., 2017). Moreover, detectable RNFL thinning by clinical OCT often reflects an already significant RGC loss and irreversible damage in glaucomatous human and rodent eyes (Kerrigan-Baumrind et al., 2000; Rovere et al., 2015; Yi et al., 2016; Schuman et al., 2020). For example, we showed that >30% of RGCs are lost before detectable RNFL thickness change 3 d after optic nerve crush (ONC) injury (Yi et al., 2016). Therefore, rather than investigating bulk RNFL thickness, we set out to examine whether we could directly monitor the changes of individual RGC axon bundles as a more sensitive and accurate indicator for RGC damage.

Clinical near-infrared (NIR) OCT systems, operating at center wavelengths from 830 to 1330 nm, cannot easily satisfy the need because of (1) axial resolution is not high enough to accurately measure minute RNFL thinning and (2) optical contrast between retinal layers is too low to measure individual RGC fiber bundle damages (Shu et al., 2017). Visible-light OCT (vis-OCT), which operates between 510 and 610 nm, offers new anatomic and functional imaging capabilities (Yi et al., 2013, 2015; Chen et al., 2017; Shu et al., 2017; Rubinoff et al., 2019). Specifically, vis-OCT provides improved axial resolution (1.3 μm in the retina) and greater optical contrast without using adaptive optics (Chong et al., 2018; Rubinoff et al., 2019; Zhang et al., 2019b). We recently established vis-OCT fibergraphy (vis-OCTF) to visualize and quantify RGC axon bundles in mice (Miller et al., 2020). This new capability enables the development of metrics, including bundle width and density, previously overlooked in mouse eyes (Miller et al., 2020).

In this study, we applied vis-OCTF to quantify and track global and regional RGC axon bundle changes in mice *in vivo*. We developed a novel circumpapillary B-scan reconstruction technique to visualize and measure the thickness of individual RGC axon bundles. These thickness measurements, combined with individual bundle width and density measurements from fibergrams, allowed us to assess RNFL health more holistically. We validated vis-OCTF's ability to detect and quantify RGC axon bundle changes in retinas with an increased number of RGCs in mice deficient in BCL2-associated X protein ($BAX^{-/-}$), and RGC damage following the ONC injury. The ONC model offers the advantage of investigating rapid RGC loss within a short time (two to four weeks; Templeton and Geisert, 2012; Puyang et al., 2016; Feng et al., 2017), which is particularly beneficial for vis-OCTF technical validation. Last, we used the RGC axon bundle width measurements gathered from our test subjects to simulate various bundle organizations and demonstrated the potential of Sholl regression coefficient estimates.

Materials and Methods

We used healthy C57BL/6 wild-type (WT), and homozygous $BAX^{-/-}$ (BAX^{tm1Sjk}, referred to as $BAX^{-/-}$, stock #002994; The Jackson Laboratory) of either sex in this study. Animal protocols were approved by the University of Virginia and Northwestern University institutional animal care and use committees. All animal protocols complied with the National Institutes of Health (NIH) guidelines.

Visual acuity and intraocular pressure (IOP) measurements

We quantified visual acuity using an optomotor response test (PhenoSys, qOMR) as reported previously (Thomson et al., 2020). Briefly, we placed each free-moving mouse on a platform surrounded by four LCD displays. After 1–2 min of gray screen adaptation, vertical black and white stripes began moving horizontally with increasing spatial frequency from 0.05 cycles/degree (c/d) to 0.5 c/d. These stripes were rotated alternating every 10 s between clockwise and counterclockwise (Rangarajan et al., 2011; Feng et al., 2013; Thomson et al., 2020). We recorded the animal's head motion using an IR-camera for further analysis (Thomson et al., 2020). For IOP measurement, we restrained the animals in a soft plastic cone and measured the IOP values from each eye using a Tonolab rebound tonometer (iCare) as described previously (Feng et al., 2013; Thomson et al., 2020).

ONC surgery

We performed the ONC procedure as described previously (Puyang et al., 2016; Yi et al., 2016; Feng et al., 2017; Liu et al., 2020). In brief, two- to six-month-old WT mice of either sex were anesthetized with an intraperitoneal injection of ketamine (114 mg/kg; Henry Schein Medical Animal Health) and xylazine (17 mg/kg; Akorn). We performed a lateral canthotomy on one eye after a small cut in the superior and lateral bulbar conjunctiva. The optic nerve was exposed through a small window made between the surrounding muscle bundles and fatty tissues and then clamped with a pair of Dumont No. 7 reverse grip tweezers (Ted Pella Inc.) for 7–10 s. After the procedure, we applied antibiotic ointment to the surgical site and monitored the mice until they were fully awake.

Vis-OCT imaging

We anesthetized the mice following the same protocol and dilated the pupils using tropicamide drops (1%; Henry Schein Medical Animal Health). During imaging, we kept the mice warm using an infrared heat lamp and applied artificial tears (1.4%; Rugby Laboratories) after each image acquisition to prevent corneal dehydration.

We imaged mice on a small animal vis-OCT system (Halo 100; Opticent Health), as previously reported (Miller et al., 2020). This system used a 1-mW illumination power on the cornea. The axial resolution was 1.3 μm in the retina, the lateral resolution was 4.5 μm at the center of the field of view (FOV), and 8.7 μm at 350 μm from the center, and the A-line rate was 25 kHz. The total vis-OCT image volume was 700 μm (x) × 700 μm (y) × 1500 μm (z). For each mouse, we acquired four vis-OCT volumes (512 A-lines/B-scan, 512 B-scans/volume) from the same eye with the ONH aligned in each of the four corners in the FOV to cover different areas of the retina. We adjusted the optical focus for each FOV if needed and processed each vis-OCT volume, as previously described (Soetikno et al., 2018). Image acquisition was guided by a built-in quality index estimator to ensure that images above a predetermined threshold were included in this study (Stein et al., 2006). After the acquisition, only montaged fibergrams with <10% missing area were included for further analysis.

We generated vis-OCT fibergrams from each vis-OCT volume (Miller et al., 2020). We used an intensity-based threshold method to detect the surface of the retina. We then cropped the RNFL by selecting the first ~16 μm in depth. Next, we calculated the mean intensity projection along the axial (z) direction to generate the fibergram image composed of RGC axon bundles and surrounding vasculature. We montaged the four images after fibergram processing for each FOV, covering ~1.2 × 1.2 mm in total. All image processing was performed using MATLAB (MathWorks, version 2019b).

We digitally resampled the four OCT volumes from each retina to generate a 400-μm radius circumpapillary scan centered on the ONH. To do so, we manually marked the ONH and plotted an 11-pixel thick ($\sim$15 μm) arc around the ONH. We sorted the pixels as a function of the angle measured between each A-line and the nasal direction with the ONH as the vertex. Adjacent A-lines were averaged within a 0.2° sector to reduce speckle noise while preserving spatial density. Last, we montaged the four arc B-scans to reconstruct a full circumpapillary scan. For 5 d after crush samples, we generated central (250 μm from ONH) and peripheral (500 μm from ONH) circumpapillary B-scans following the same protocol.

Traditional circumpapillary scans in the mouse retina were acquired along a continuous circular path centered on the ONH (Soetikno et al., 2018). However, such a scan pattern does not consistently scan orthogonally to the axon bundles throughout the entire B-scan, which causes the signal intensity from the axon bundles to fluctuate because of low bundle reflectance in certain regions of the scan. More importantly, this scan pattern does not ensure perfect centering of the ONH, which may lead to measurement error. A comparison between the traditionally acquired circumpapillary scan and circumpapillary scan resampled from the rectangular scan is shown in Extended Data Figure 1-1. The path of the resampled scan is shown in red, and the estimated path of the traditionally acquired circumpapillary scan is shown in blue (Extended Data Fig. 1-1*A*). The reconstructed B-scan images are shown in Extended Data Figure 1-1*B* for the resampled scan (top panel) and traditional scan (bottom panel). Compared with the traditional scan, individual RGC axon bundles in the resampled scan can be clearly visualized throughout the entire B-scan. As shown in Extended Data Figure 1-1*C*, RGC axon bundle thickness measurements from the resampled scan have a 25% lower SD than measurements from the traditional circumpapillary B-scan, which could be explained by the reduced speckle noise, precise centering on the ONH, and/or maximized reflectance from the bundles in the resampled scan.

RGC axon bundle organization analysis

We recently established a novel technique based on semi-log Sholl analysis for analyzing the RGC axon bundle network (Miller et al., 2020). This technique consists of drawing concentric circles centered on the ONH, and counting the number of RGC axon bundles intersections (N) along each circle with the radius (r). After normalizing the number of intersections by the area of each circle (A) and plotting on a semi-log axis as a function of radius, we used a first-order polynomial fit to estimate the Sholl regression coefficient (k). This relationship can be summarized as $\log(N/A) = -kr + m$, where m describes the initial bundle density. RGC axon bundle networks with a more rapid decrease in bundle density with the distance from the ONH will have a higher k value than networks with a slower decrease. We analyzed each fibergram with a radius range of 250–450 μm and incremented each circle by one pixel ($\sim$1.4 μm), resulting in a total of 142 analysis circles.

RGC axon bundle size quantification

We measured the thickness of the retina, ganglion cell-IPL (GCIPL) and individual RGC using ImageJ (Fig. 1*A-B*). The overall retinal thickness was measured as the distance between the vitreous/RNFL and RPE/choroid boundary, as indicated in Figure 1*B*, green arrows. The thickness of GCIPL was a measure between the top edge of the vitreous/RNFL and the bottom edge of the IPL, as indicated in Figure 1*B*, blue arrows. To keep the measurement technique consistent for all structures, we sampled the retinal and GCIPL thickness at evenly spaced intervals ($\sim$150 μm). The thickness of the RGC axon bundles was measured as the center thickness of each bundle (highlighted in Fig. 1*B*, orange arrows). The number of individual measurements for retina, RGC axon bundle, and GCIPL thickness is thus presented rather than the number of mice.

To measure the RGC axon bundles' width, we first manually selected axon bundles located $\sim$400 μm from the ONH in the fibergram images (highlighted in Extended Data Fig. 2-1*A*, red dots). We manually marked the center axis of the bundle for each selected point and plotted the average intensity profile orthogonal to the center axis, as shown in Extended Data Figure 2-1*B*. Extended Data Figure 2-1*C* shows the normalized average intensity profile of the selected axon bundle, and we used the full width at $1/e^2$ as the bundle width. We measured the RGC axon bundle widths at 250 μm (central) and 500 μm (peripheral) from the ONH 5 d after ONC. Blood vessels appeared as dark shadows in the B-scan images and had uniquely distinguishable branching structures compared with surrounding axon bundles in fibergram images. Therefore, they were easily excluded from analysis.

Immunohistochemistry and confocal microscopy

After acquiring vis-OCT data, we euthanized the mice with Euthasol (15.6 mg/ml; Virbac) and perfused them with 4% paraformaldehyde (PFA) in PBS (Miller et al., 2020). We then enucleated the eyes and marked the orientations. The eyecups were fixed in PFA for 30 min and blocked in 5% donkey serum with 2.5% BSA and 0.5% Triton X-100 in Tris-buffered saline (pH 7.5) for 2 h at room temperature. The primary antibody, anti-Tuj-1 (1:200; a gift from Anthony J. Spano; Miller et al., 2020), was incubated overnight at 4°C and secondary antibody, donkey anti-mouse immunoglobulin G conjugated to Alexa Fluor TM 488 (1:1000; ThermoFisher Scientific), was incubated overnight at 4°C. The retinas were flat mounted and coverslipped with Vectashield mounting medium (Vector Laboratories Inc.; Feng et al., 2013; Miller et al., 2020). Confocal microscopy was performed using the 3D Z-stack mode on a Zeiss LSM 800 microscope (Carl Zeiss AG; Miller et al., 2020; Thomson et al., 2020). At least 25 tiles across the whole retina were imaged to cover a total volume of 5.99 mm (x) × 5.88 mm (y) × 30 μm (z) at a pixel size of 1.24 μm/pixel. Z-stack slices were then projected to create 2D en face confocal microscopy images.

Experimental design and statistical analyses

All statistical analyses were performed using MATLAB. We used a linear mixed-effects model for all thickness and width comparisons to remove influence from individual subjects. We used t tests to compare Sholl analysis data. For BAX experiments, we used unpaired t tests, and for ONC experiments, we used paired t tests. The Spearman correlation coefficient (ρ) was used for comparing confocal and vis-OCT bundle width measurements. A significance level of 0.05 was used for all statistical comparisons unless specified otherwise. All results were reported as mean ± SD.

Results

BAX$^{-/-}$ mice have increased retinal and RGC axon bundle layer thickness

The RNFL thickness is not a sensitive biomarker for RGC survival as discussed in the introduction. Therefore, we analyzed the RGC axon bundle thickness directly by taking advantage of vis-OCT's high axial resolution and our novel postprocessing technique for enhancing axon bundle visualization in B-scan images. BAX$^{-/-}$ mice exhibit an increased number of RGCs by >200% in adults by preventing developmental cell death (Libby et al., 2005; Maes et al., 2017). Thus, BAX$^{-/-}$ mice have thicker and more densely distributed RGC axon bundles. We tested whether we could detect an increased overall retinal thickness, GCIPL thickness, and RGC axon bundle layer thickness using the resampled circumpapillary B-scans (Fig. 1*A*). The red arrows overlaid on the fibergrams show the resampled circumpapillary scan path, and the blue arrow indicates the left-most A-line in the resampled B-scans. The magnified B-scans in Figure 1*B* highlight the dramatic difference in retinal structure for BAX$^{-/-}$ mice compared with the littermate control group. The average overall retinal thickness in BAX$^{-/-}$ mice was 261.4 ± 8.5 μm (n = 133), which is significantly thicker (17%) compared with littermate controls (220.3 ± 6.1 μm, n = 166, p = 1.9.0e-49; Fig. 1*C*). The GCIPL thickness in BAX$^{-/-}$ mice was also significantly thicker (34%) compared with the controls (BAX$^{-/-}$: 89.7 ± 5.9 μm, n = 232; CTRL: 63.4 ± 3.2 μm, n = 218; p = 2.6e-100; Fig. 1*D*). Importantly,

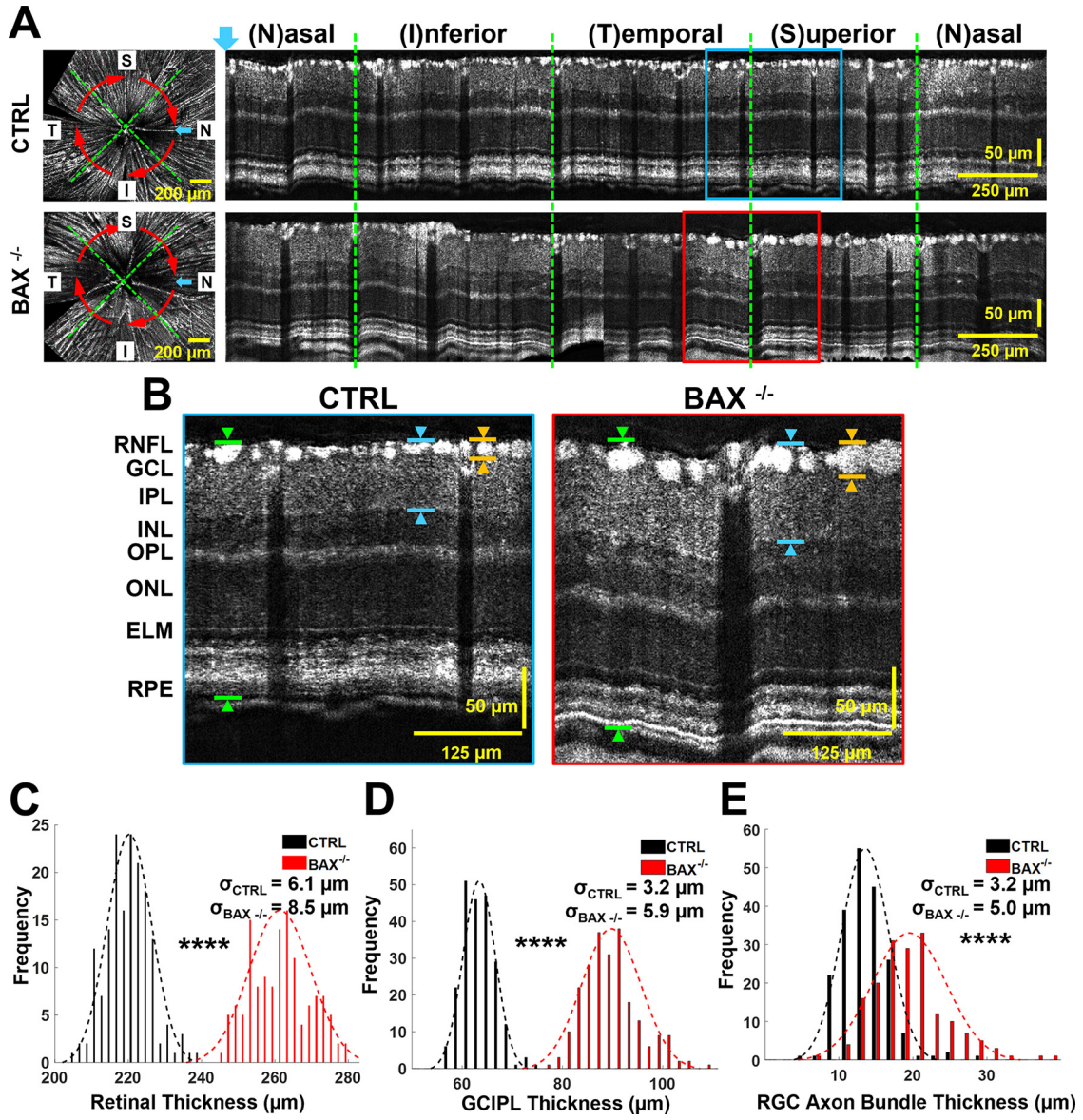

Figure 1. BAX knock-out mice ($BAX^{-/-}$) showed increased retinal and RGC axon bundle thickness. ***A***, Example fibergrams (left panels) and circumpapillary B-scans (right panels) of littermate controls ($BAX^{+/+}$ and $BAX^{+/-}$, labeled as CTRL; top panel) and $BAX^{-/-}$ (bottom panel). The blue arrow highlights the left-most A-line of circumpapillary B-scans, and the red arrows indicate the direction and location of reconstructed circumpapillary B-scans. ***B***, Magnified view of the boxed regions indicated in panel ***A***. INL: inner nuclear layer; OPL: outer plexiform layer; ONL: outer nuclear layer; ELM: external limiting membrane; and RPE: retinal pigment epithelium. The green arrows exemplify retinal thickness measurements, the blue arrows exemplify the GCIPL measurements, and the orange arrows exemplify RGC axon bundle measurements. ***C***, Distribution of retinal thickness measurements for CTRL (black) and $BAX^{-/-}$ (red) mice. ***D***, GCIPL thickness measurements for CTRL (black) and $BAX^{-/-}$ (red) mice. ***E***, RGC axon bundle thickness measurements for CTRL (black) and $BAX^{-/-}$ (red) mice (****$p < 0.0001$); σ values represent SD. Extended Data Figures 1-1, 1-2 are for Figure 1.

the RGC axon bundle layer in $BAX^{-/-}$ mice was significantly thicker (36%) compared with the controls ($BAX^{-/-}$: 19.5 ± 5.0 μm, $n = 174$; CTRL: 13.5 ± 3.2 μm, $n = 201$; $p = 1.2e\text{-}35$; Fig. 1*E*).

Histograms were generated from the data by grouping measurements into 2-μm wide bins. The overall retinal thickness distributions shown in Figure 1*C* indicate significantly greater retinal thickness for $BAX^{-/-}$ mice with greater variation compared with their littermate controls ($BAX^{-/-}$: $n = 5$; CTRL: $n = 4$ mice). Interestingly, although there are more RGCs in adult $BAX^{-/-}$ ($n = 5$), they exhibited a dramatic loss in visual acuity, compared with $BAX^{+/+}$ ($n = 4$) and $BAX^{+/-}$ mice ($n = 4$; $p < 0.0001$, one-way ANOVA; Extended Data Fig. 1-2*A*). We also tested the IOP, which could affect retinal function, and found no significant difference among the three groups (Extended Data Fig. 1-2*B*). Because there was no significant difference between $BAX^{+/+}$ and $BAX^{+/-}$ mice, we combined them into one control group (CTRL) for the remainder of the study.

Vis-OCTF revealed increased RGC axon bundle width and slower change in bundle density in $BAX^{-/-}$ mice

The montaged vis-OCT fibergram images of a CTRL and $BAX^{-/-}$ mouse are shown in Figure 2*A*, top and bottom panels, respectively. Immediately following vis-OCT imaging, the same retinas were immunostained with Tuj-1 for RGC axons and imaged by confocal microscopy. Side-by-side comparison of the vis-OCT fibergram and confocal images of the same retinas confirmed that the RGC axon bundle organization was captured similarly by both *in vivo* and *ex vivo* imaging methods. The

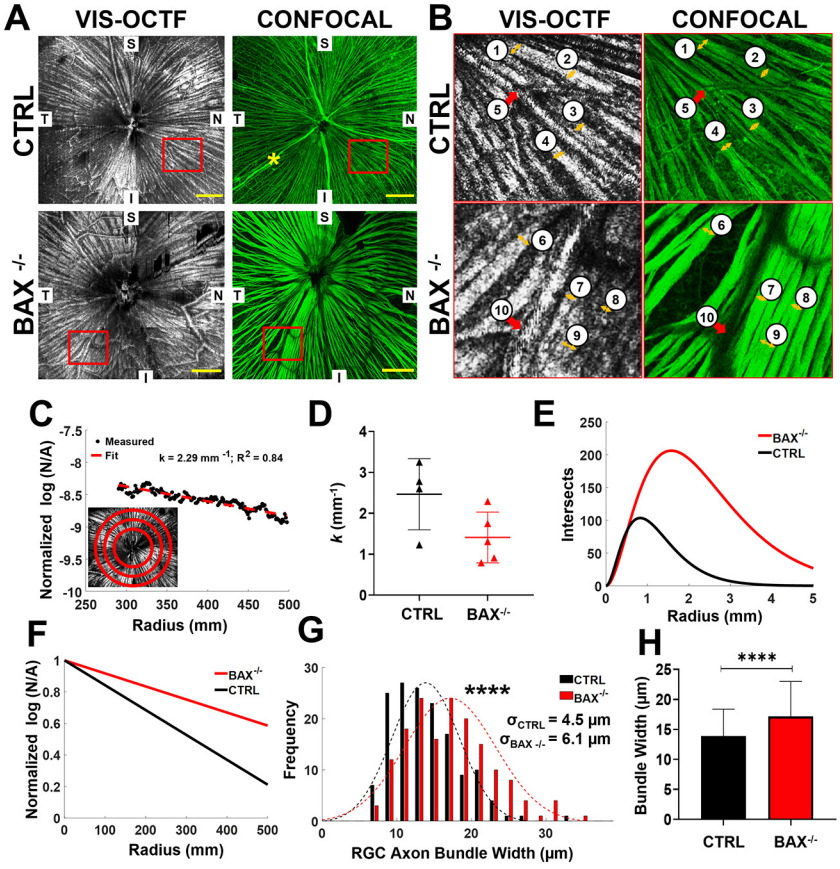

Figure 2. Vis-OCTF revealed BAX$^{-/-}$ mice had increased RGC axon bundle width and density. ***A***, Comparing mouse RGC axon bundle organization between CTRL (top panels) and BAX$^{-/-}$ (bottom panels) retinas using *in vivo* vis-OCTF (left panels) and *ex vivo* confocal microscopy imaging of flat-mounted retinas immunostained for RGC axons (right panels). ***B***, Magnified view of highlighted areas in panel ***A*** (red boxes). The orange arrows indicate RGC axon bundles, and the red arrows indicate blood vessels. The widths of individual axon bundles were measured (also see Extended Data Fig. 2-1 and Results). ***C***, An example plot of the semi-log Sholl regression analysis using the fibergram image of a control retina shown in the inset. ***D***, Measured *k* values for CTRL (black triangles) and BAX$^{-/-}$ (red triangles) mice. ***E***, The average number of RGC axon bundles (intersects) recorded as a function of distance from the ONH (radius) for CTRL (black) and BAX$^{-/-}$ (red) mice. ***F***, Average *k* value for CTRL (black) and BAX$^{-/-}$ (red) mice represented as slope of semi-log Sholl regression plot. ***G***, Distribution of RGC axon bundle width measurements for CTRL (black) and BAX$^{-/-}$ (red) mice; σ values indicate SD. ***H***, Average RGC axon bundle width for CTRL (black) and BAX$^{-/-}$ (red) mice (****$p < 1e\text{-}4$); σ values represent SD. Yellow scale bars: 250 μm; blue scale bars: 100 μm; S: superior; N: nasal; T: temporal; I: inferior. Extended Data Figure 2-1 is for Figure 2.

magnified view of the areas highlighted in Figure 2*A*, red boxes, demonstrates how RGC axons in the BAX$^{-/-}$ (bottom panels) group form large bundles compared with the CTRL mice (Fig. 2*B*, top panels).

We quantified the change in RGC axon bundle density with distance from the ONH using semi-log Sholl analysis (Miller et al., 2020), as shown in Figure 2*C*. The average Sholl regression coefficient, *k*, for BAX$^{-/-}$ mice is decreased compared with the CTRL mice (CTRL: 2.5 ± 0.9 mm^{-1}, $n = 4$ mice; BAX$^{-/-}$: 1.4 ± 0.2 mm^{-1}, $n = 5$ mice; $p = 0.07$, unpaired *t* test), indicating a slower change in RGC axon bundle density moving outward from the ONH to the periphery. Figure 2*E* shows the projected number of RGC axon bundle intersects based on the average *k* values for the BAX$^{-/-}$ and CTRL mice. Figure 2*F* shows the average normalized semi-log Sholl regression plots for BAX$^{-/-}$ (red line) and CTRL (black line) mice. BAX$^{-/-}$ mice have a lower slope than CTRL mice, indicating a slower change in axon bundle density moving outward from the ONH.

Next, we characterized the RGC axon bundle size by measuring lateral bundle width in the fibergram at 400 μm from the ONH (Extended Data Fig. 2-1). The orange arrows in Figure 2*B* indicate axon bundles and red arrows indicate blood vessels, which appeared in the confocal images because of non-specific immunostaining, denoted by the asterisk in Figure 2*A*. The widths of the axon bundles in the CTRL fibergram are (1) 22 μm, (2) 21 μm, (3) 18 μm, and (4) 20 μm (Spearman correlation coefficient $\rho = 0.74$), whereas the axon bundles in the BAX$^{-/-}$ fibergram (6–8) correspond to widths of (6) 25 μm, (7) 22 μm, (8) 26 μm, and (9) 35 μm ($\rho = 0.73$). Figure 2*G* shows the distribution of the lateral RGC axon bundle widths measured from the BAX$^{-/-}$ (red bars) and CTRL (black bars) mice, which indicates an increase in axon bundle width for the BAX$^{-/-}$ mice compared with the CTRL mice (BAX$^{-/-}$: $n = 5$ mice; CTRL: $n = 4$ mice). The average axon bundle width (Fig. 2*H*) was significantly larger (21%) in BAX$^{-/-}$ mice (17.1 ± 6.1 μm, $n = 162$) compared with controls (13.9 ± 4.5 μm, $n = 151$; $p = 1.4e\text{-}7$).

Retina and RGC axon bundle size decreased, and bundle density decreased more rapidly 12 d after ONC injury

We assessed vis-OCTF's ability to detect RGC axon bundle damage following ONC injury. Figure 3*A* shows the example fibergrams and circumpapillary B-scan images before and 12 d after ONC. The red circular arrows on the fibergrams show the path of the resampled circumpapillary scan, and the blue arrow indicates the leftmost A-line in the resampled B-scan.

We quantified retinal and RGC axon bundle thickness before and after ONC injury. Figure 3*B* shows a magnified view of the boxes in Figure 3*A* before (blue box) and 12 d after ONC (red box). As seen in the magnified B-scans, there was a significant reduction in overall retinal thickness (green arrows), as well as GCIPL (blue arrows) and bundle thickness (orange arrows) after ONC. Further, the retinal tissue appeared thinner and uneven, and the RGC axon bundles presented faint and smaller bundles at 12-d after ONC (Fig. 3*B*). Before ONC, the retinal thickness was 219.1 ± 4.2 μm ($n = 196$), and at 12 d after ONC, the retinal thickness decreased by 2% to 215.6 ± 10.2 μm ($n = 169$; $p = 7.5e\text{-}6$). Similarly, the GCIPL thickness decreased by 12% at 12 d after ONC (before ONC: 59.1 ± 3.6 μm, $n = 280$; after ONC: 51.9 ± 5.7 μm, $n = 243$, $p = 1.1e\text{-}71$; Fig. 3*D*). The distribution plot in Figure 3*E* also indicates a significant decrease in RGC axon bundle thickness at 12 d after ONC. Before ONC, the RGC axon bundle thickness was 12.6 ± 3.1 μm ($n = 278$), and 12 d after ONC the bundle thickness was 11.3 ± 2.7 μm ($n = 218$), corresponding to a 10% reduction ($p = 1.7e\text{-}6$). Together the results indicate the thickness of the retina, GCIPL, and RGC axon bundles was significantly reduced 12 d after ONC with greater variation. The greater retinal thickness variation may be partially

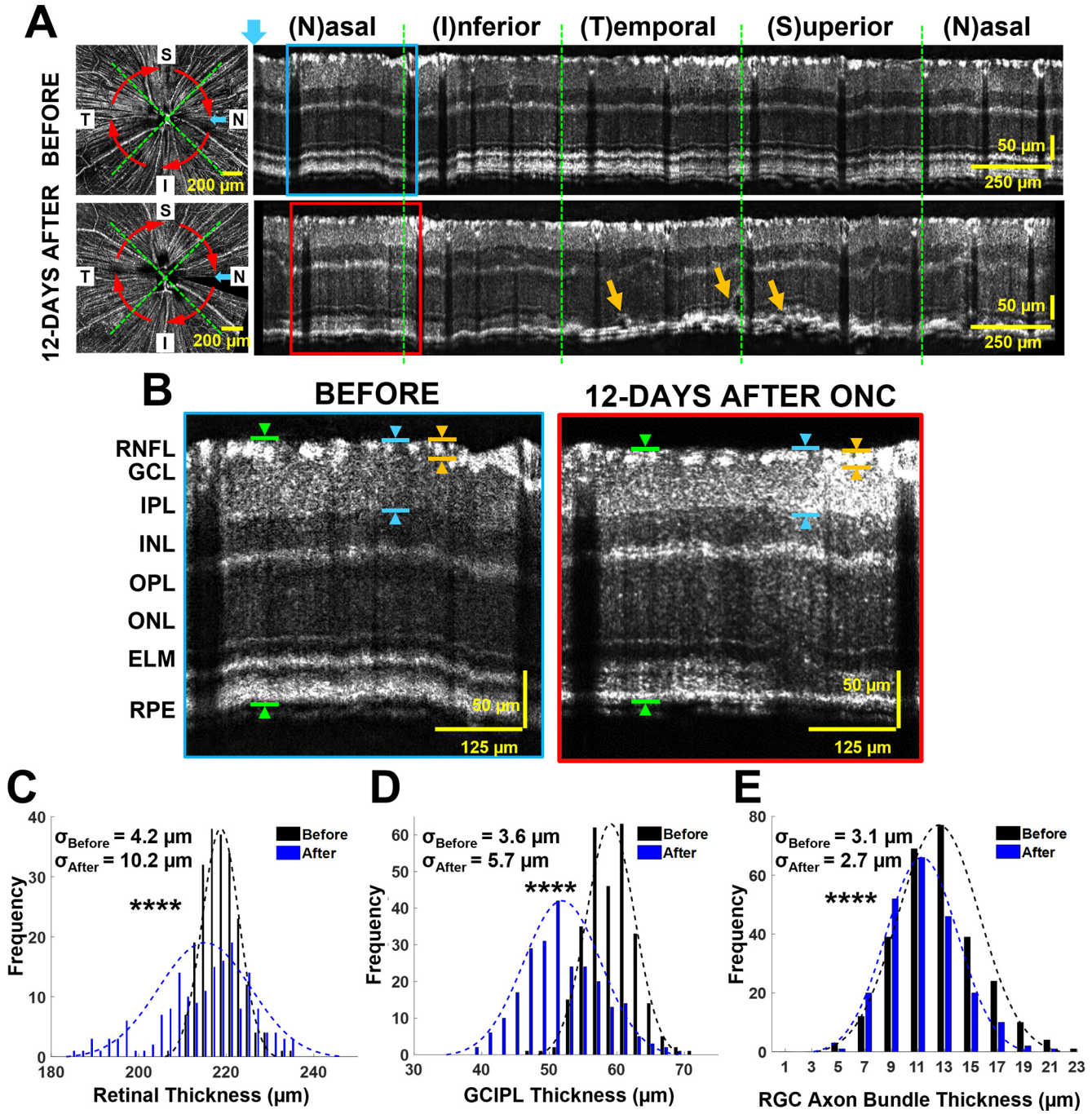

Figure 3. At 12 d after ONC injury, mice exhibited reduced retinal and RGC axon bundle thickness. ***A***, Fibergrams and circumpapillary B-scans before (top panels) and 12 d after ONC (bottom panels). The blue arrow indicates the left-most A-line in circumpapillary B-scans, and the red arrows indicate the direction and location of reconstructed circumpapillary B-scans. The orange arrows in the bottom panel indicate localized edema. ***B***, Magnified view of boxed regions indicated in panel ***A***. The green arrows exemplify retinal thickness measurement, the blue arrows exemplify the GCIPL measurements, and the orange arrows exemplify RGC axon bundle thickness measurement. ***C***, Distribution of retinal thickness measurements in retinas before (black) and 12 d after crush (blue). ***D***, GCIPL measurements in retinas before (black) and 12 d after crush (blue). ***E***, RGC axon bundle thickness measurements in retinas before (black) and 12 d after crush (blue; $^{****}p < 0.0001$); σ values represent the SD of distributions.

attributed to the formation of edema, as indicated in Figure 3*A*, orange arrows.

To quantify the detailed changes in the RGC axon bundle layer, we compared the montaged post-ONC vis-OCT fibergrams with their corresponding confocal images of flat-mounted retinas, immunostained for RGC axons. Figure 4*A*, top panel, shows the *in vivo* fibergram before ONC (left panel), *in vivo* fibergram 12 d after crush (middle panel), and *ex vivo* confocal microscopy image acquired after vis-OCT imaging on the 12th day after ONC (right panel). Retina orientation was tracked by dividing the en face RGC axon bundle images into superior (S), inferior (I), nasal (N), and temporal (T) quadrants. The magnified views, indicated by red boxes in the top panel of Figure 4*A*, are shown in Figure 4*A*, bottom panels, in which the orange arrows (1–4) highlight axon bundles and the red arrows (5 and 6) highlight blood vessels. We compared the *k* values at 12 d after ONC in vis-OCTF and confocal microscopy and found they agree with each other (vis-OCTF: 3.0 ± 0.4 mm^{-1}, $n = 5$;

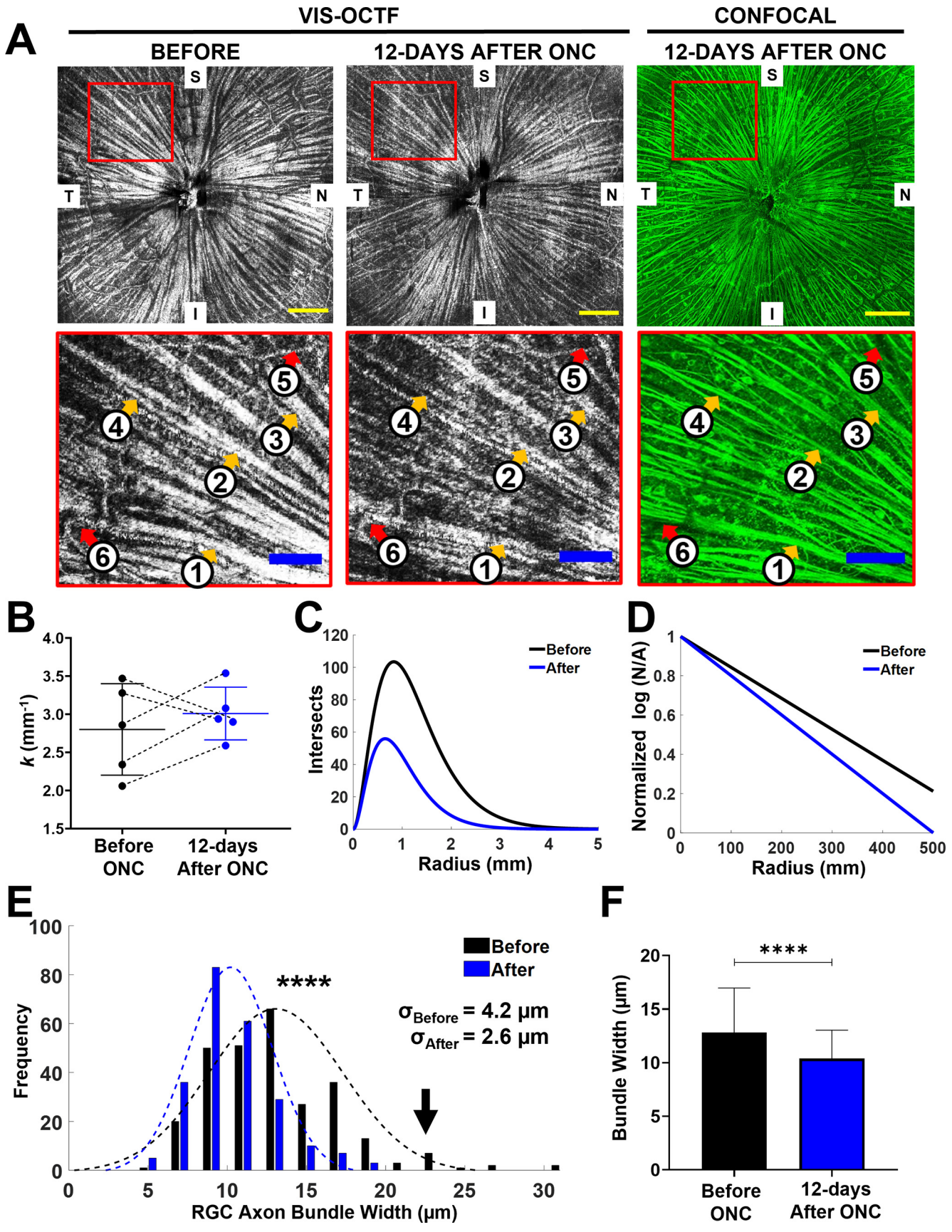

Figure 4. *In vivo* tracking of RGC axon bundle organization by vis-OCTF revealed a reduction in both axon bundle width and density at 12 d after ONC. ***A***, Comparing RGC axon bundle organization before (left panels) and after crush (middle and right panels) *in vivo* with vis-OCTF (left and middle panels) and *ex vivo* with confocal microscopy images of flat mounted retinas stained for RGC axons (right panels). Bottom panels show the magnified views of highlighted regions in top panels (red boxes). The orange arrows in the bottom panels indicate axon bundles, and the red arrows indicate blood vessels. Yellow scale bars: 250 μm; blue scale bars: 100 μm. ***B***, Tracking the *k* values for individual retinas before (black) and after crush (blue). ***C***, The average

confocal: 2.9 ± 0.3 mm^{-1}, $n = 5$). The mean k value was changed from 2.8 ± 0.6 mm^{-1} before ONC ($n = 5$) to 3.0 ± 0.4 mm^{-1} after ONC ($n = 5$ mice; $p = 0.53$, paired t test; Fig. 4*B*). Of the five mice we tracked, three mice showed an increase, and two showed a decrease in their k values following ONC injury. Figure 4*D* shows the averaged semi-log Sholl regression plots for mice before (black) and after ONC (blue). As demonstrated in Figure 4*D*, the blue line corresponds to a higher slope than the black line in the semi-log Sholl regression plot, suggesting an overall fast decrease in RGC axon bundle density moving outward from the ONH following ONC injury.

We observed a 25% reduction in RGC axon bundle width 12 d after ONC. This decrease is further detailed in Figure 4*A*, bottom panels, where the widths of bundles 1–4 decreased after ONC (1) 28.4–23.3 μm, (2) 22.2–14.0 μm, (3) 22.8–18.5 μm, and (4) 17.1–15.6 μm. Additionally, the bundle width measurements 12 d after ONC agreed well with the confocal microscopy width measurements (ρ = 0.79). We further quantified the axon bundle width for all five mice and plotted their distribution before and after ONC in Figure 4*E*. As indicated by the distribution curves, the RGC axon bundle width is significantly reduced 12 d after ONC (blue) compared with before (black; before ONC: 13.1 ± 4.2 μm, $n = 279$; after ONC: 10.2 ± 2.6 μm, $n = 234$; $p = 6.7e\text{-}18$). Together, at 12 d after ONC, the RGC axon bundles showed 10% and 25% reduction in thickness and width, respectively.

Regional changes in axon bundle thickness were observed 5 d after ONC injury

Previous studies observed overall RNFL thickness exhibited no significant change in the first week after ONC, despite substantial RGC loss (Feng et al., 2013; Yi et al., 2016; Huang et al., 2017). In addition, because the partial ONC procedure may produce uneven optic nerve damage in individuals (Liu et al., 2020), we tested whether we could quantify and track regional changes in axon bundle thickness following ONC. We divided our thickness analysis into eight regions, consisting of four retinal quadrants at 250 μm (central) and 500 μm (peripheral) from the ONH (Fig. 5*A*). For each region, we generated a resampled circumpapillary B-scan and measured overall retinal and axon bundle thickness, as described in Materials and Methods. Figure 5*B* shows an example of resampled B-scans for one eye before (left panels) and 5 d after ONC (right panels) in the central (top panels), and peripheral (bottom panels) analysis regions.

We grouped thickness measurements from all six mice to determine whether thickness changes at 5 d after ONC depend on the distance from the ONH. The overall retinal thickness distributions in the central and peripheral analysis regions are shown in Figure 5*C*,*D*. We observed a 3% reduction in retinal thickness 5 d after ONC in the central region (before ONC: 215.8 ± 4.5 μm, $n = 312$; after ONC: 209.5 ± 7.5 μm, $n = 238$; $p = 5.8$–42). Conversely, we found a 1% increase in retinal thickness 5 d after ONC in the peripheral region (before ONC: 220.0 ± 4.9 μm, $n = 515$; after ONC: 221.4 ± 7.2 μm, $n = 436$; $p = 2.3e\text{-}4$). The GCIPL thickness distributions in the central and peripheral analysis regions are shown in Figure 5*E*,*F*. A decrease (3%) in GCIPL thickness 5 d after ONC was found in the central region (before ONC: 62.6 ± 4.6 μm, $n = 340$; after ONC: 60.7 ± 5.7 μm, $n = 219$; $p = 1.0e\text{-}5$). In the peripheral region, the GCIPL followed the same trend, a thinning (5%) of the GCIPL was found after ONC (before ONC: 60.1 ± 3.7 μm, $n = 387$; after ONC: 57.3 ± 4.0 μm, $n = 331$; $p = 1.1e\text{-}23$). The RGC axon bundle thickness distributions of the central and peripheral analysis regions are shown in Figure 5*G*,*H*, respectively. There was no significant change in axon bundle thickness in the central region 5 d after ONC (before ONC: 17.1 ± 4.3 μm, $n = 299$; after ONC: 17.4 ± 5.6 μm, $n = 213$; $p = 0.55$). However, there was a 5% increase in axon bundle thickness in the peripheral region after ONC (before ONC: 13.0 ± 3.2 μm, $n = 410$; after ONC: 13.7 ± 3.5 μm, $n = 395$; $p = 2.0e\text{-}3$).

To further characterize the local changes in RGC axon bundle thickness, we generated thickness heatmaps for the eight analysis regions in each retina. Example heatmaps for two different eyes are shown in Figure 6*A*,*B*. The left heatmaps show mean bundle thickness before ONC, the middle heatmaps show mean bundle thickness after ONC, and the right heatmaps show the relative change in bundle thickness before and after ONC. The relative change heatmap in Figure 6*A* shows a significant increase in bundle thickness in the central temporal quadrant ($p = 2.2e\text{-}3$, unpaired t test) and the peripheral nasal quadrant ($p = 0.03$, unpaired t test). The relative change heatmap in Figure 6*B* shows a decrease in bundle thickness in the central inferior quadrant ($p = 0.03$, unpaired t test). These results show that we could detect the local changes in RGC axon bundles, highlighting the potential for *in vivo* tracking of region-dependent changes in the neural retina following disease insult in individuals.

RGC axon bundle width reduced, but no change in bundle density 5 d after ONC injury

We compared the vis-OCT fibergrams before and 5 d after ONC for six mice. Figure 7*A* shows example fibergrams for one eye before (left panel) and 5 d after ONC (right panel). At 5 d after ONC, the RGC axon bundles in the fibergram appeared thinner and less reflective than before ONC. For example, the widths of the axon bundles labeled 1–4 in Figure 7*A* decreased as follows: (1) 26.0–27.0 μm, (2) 23.3–18.9 μm, (3) 35.0–32.9 μm, and (4) 11.0–10.8 μm.

Next, we compared the RGC axon bundle width in the central and peripheral analysis regions. The axon bundle width distribution in the central region (Fig. 7*C*) shows a 13% reduction in bundle width 5 d after crush (before ONC: 11.8 ± 3.0 μm, $n = 142$; after ONC: 10.3 ± 2.8 μm, $n = 133$; $p = 1.5e\text{-}5$). In the peripheral region, bundle width reduced by 12% after ONC (before ONC: 12.1 ± 3.2 μm, $n = 316$; after ONC: 10.6 ± 2.7 μm, $n = 300$; $p = 6.9e\text{-}10$). The distribution in Figure 7*C*,*D* showed that the variation in width did not change much before and after ONC, suggesting a more uniform reduction in bundle width in both central and peripheral regions.

We further analyzed fibergram images using Sholl analysis. Although no significant difference was detected, the Sholl regression was changed from 2.9 ± 0.4 mm^{-1} before ONC ($n = 6$) to 2.5 ± 0.7 mm^{-1} after ONC ($n = 6$; $p = 0.07$, paired t test; Fig. 7*B*). This result suggests that the RGC axon bundle density pattern may not change significantly with increasing distance from the ONH. Taken together, we observed location-dependent changes in RGC axon bundle thickness at 5 d after ONC injury, a 2% increase in RGC axon bundle thickness and a 13% reduction in

←

number of RGC axon bundles (intersects) recorded as a function of distance from the ONH (radius) for mice before and after ONC. ***D***, Average k value for mice before and after ONC represented as slope of semi-log Sholl regression plot. ***E***, Distribution of RGC axon bundle width measurements for mice before and after ONC; σ values indicate SD. The black arrow points to that large bundles disappeared after ONC. ***F***, Average RGC axon bundle width for mice before and after ONC (****$p <$ 1e-4).

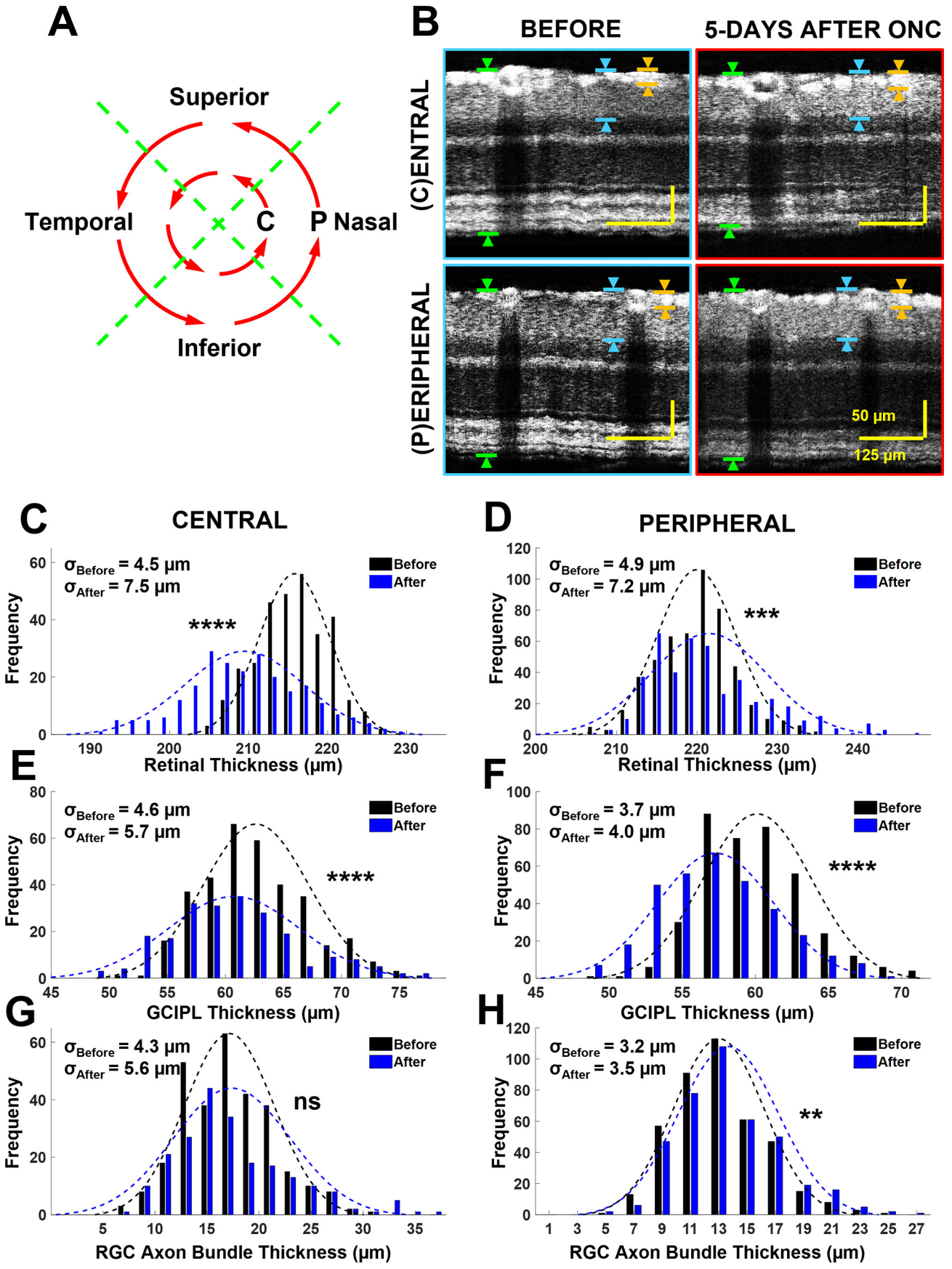

Figure 5. Regional thickness measurements showed changes in RGC axon bundle thickness at 5 d after ONC. ***A***, Schematic representation of eight retinal regions from which RGC axon bundle thickness was measured. Measurements were recorded in each retinal quadrant near the center (C, 250 μm from the ONH) and in the periphery (P, 500 μm from the ONH). ***B***, Example circumpapillary B-scan sections taken near the center (top panels) and periphery (bottom panels) before (left panels) and 5 d after (right panels) ONC. The green arrows exemplify retinal

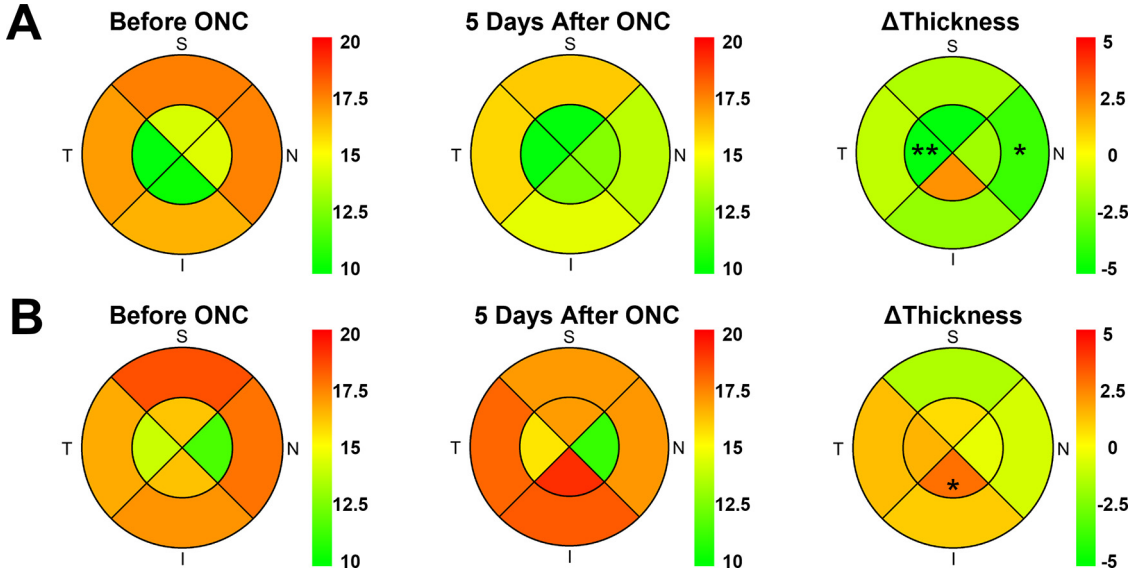

Figure 6. Heatmaps revealed location-dependent changes in RGC axon bundle thickness. Heatmaps from two example mice (***A***, mouse #1; and ***B***, mouse #2) show the mean thickness of RGC axon bundles before crush (left), after crush (middle), and change in thickness (right; $*p < 0.05$, $**p < 0.01$).

width in the central retina, and a 5% increase in thickness and a 12% reduction in width in the peripheral retina.

Modeling the organization of RGC axon bundle network

We performed a simulation to better understand the relationship between the axon bundle parameters and the measured k values. The layout of the RGC axon bundles was simulated by randomly plotting lines of various thickness uniformly distributed about the center of a 1.5×1.5 mm area. We then tuned the size and number of the simulated bundles independently and measured the k value. Each simulation was repeated 20 times. Examples of bundle distributions are shown in Figure 8*A*.

First, we varied the number of bundles by 20% from a baseline of 250 bundles. The baseline plots resulted in a k value of 2.9 ± 0.3 mm^{-1} ($n = 20$) and increasing the number of bundles resulted in a 21% decrease in k (2.3 ± 0.3 mm^{-1}, $n = 20$). Conversely, reducing the number of bundles resulted in a 21% increase in k (3.5 ± 0.4 mm^{-1}, $n = 20$). Next, we varied the thickness by 20% from a baseline of 13 μm. Increasing the thickness resulted in a 21% decrease in k (2.3 ± 0.4 mm^{-1}, $n = 20$), whereas decreasing the thickness resulted in a 28% increase (3.7 ± 0.2 mm^{-1}, $n = 20$).

These k value changes are reflected as changing slopes in the semi-log Sholl regression plot in Figure 8*B*. In increased bundle number and thickness, the slopes are decreased compared with the CTRL. This result suggests a more gradual change in bundle density moving outward from the ONH. Conversely, when the axon bundles are fewer and thinner, the slope is greater than the baseline, suggesting a sharper change in bundle density moving outward from the ONH to the periphery.

The overall number of intersects as a function of radius is shown in Figure 8*C*. As expected, when more bundles are added, the number of detected bundles at each radius increases, and when fewer bundles are present, decreases. However, when the number of bundles is held constant and the thickness is varied, the overall number of counted bundles changes. Furthermore, the number of simulated bundles is not reflected in the total number of bundle intersects. This occurs for two reasons: (1) when bundles are touching, they are only counted as one bundle, and (2) when a bundle is too small (below the lateral resolution), it does not get counted.

Finally, we repeated the simulation using actual RGC axon bundle width measurements from the WT, BAX$^{-/-}$, and ONC (5 and 12 d after crush) mice presented in this study. For each condition, we tuned the number of simulated bundles until the simulated k values fell within the range of the measured k value. The number of RGC axon bundles for each condition was 250 (WT), 280 (BAX$^{-/-}$), 300 (12 d after crush), and 300 (5 d after crush). The k values for each condition are presented side by side in Figure 8*D*. Both measured (k_m) and simulated (k_s) k values agreed with each other for the CTRL mice ($k_m = 2.7 \pm 0.6$ mm^{-1}, $n = 15$; $k_s = 2.7 \pm 0.3$ mm^{-1}, $n = 20$; $p = 0.98$, unpaired t test). BAX$^{-/-}$ mice had thicker and more RGC axon bundles resulting in lower k values ($k_m = 1.4 \pm 0.6$ mm^{-1}, $n = 5$; $k_s = 1.7 \pm 0.3$ mm^{-1}, $n = 20$). In the case of ONC mice, the bundles became narrower and began to separate from each other, resulting in higher k values at 12 d after crush ($k_m = 3.0 \pm 0.3$ mm^{-1}, $n = 5$; $k_s = 3.1 \pm 0.2$ mm^{-1}, $n = 20$; $p = 0.42$, unpaired t test) and at 5 d after crush ($k_m = 2.4 \pm 0.6$ mm^{-1}, $n = 5$; $k_s = 3.0 \pm 0.2$ mm^{-1}, $n = 20$; $p = 0.09$, unpaired t test).

Discussion

Vis-OCT could improve the detection and management of RGC damage in glaucoma

Vis-OCT operates from 510 to 610 nm (Yi et al., 2013, 2015; Chen et al., 2017; Shu et al., 2017, 2019; Soetikno et al., 2018; Rubinoff et al., 2019), where the optical scattering coefficients of biological tissues are much higher than the NIR spectral range. As a result, vis-OCT offers new anatomic and functional imaging

←

thickness measurements, the blue arrows exemplify the GCIPL measurements, and the orange arrows exemplify RGC axon bundle thickness measurements. ***C***, ***D***, Distribution of retinal thickness measurements from the central (***C***) and the peripheral regions (***D***). ***E***, ***F***, GCIPL thickness measurements from the central (***E***) and the peripheral regions (***F***). ***G***, ***H***, RGC axon bundle thickness measurements from the central (***G***) and the peripheral regions (***H***; NS: not significant, $p > 0.05$; $**p < 0.01$, $***p < 0.001$, $****p < 0.0001$); σ values in all distribution plots denote SD.

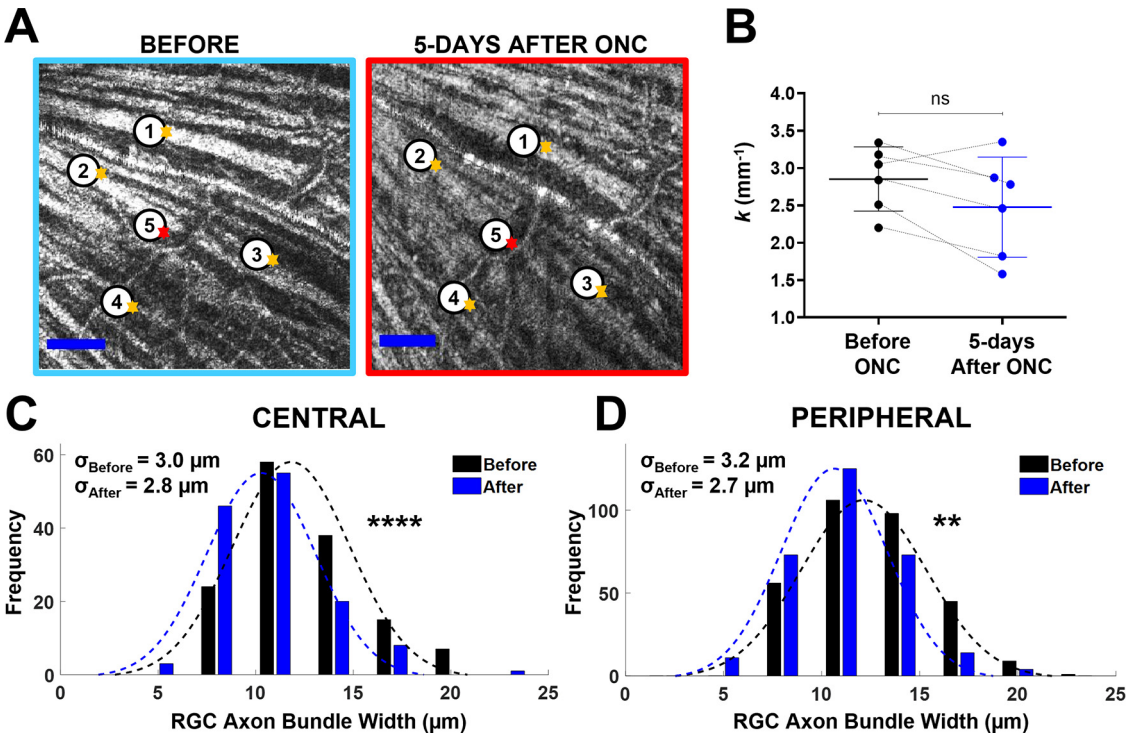

Figure 7. At 5 d after ONC, RGC axon bundle width reduced, but no change in bundle density. ***A***, vis-OCT fibergrams before (left) and 5 d after (right) ONC. The orange arrows indicate RGC axon bundles, and the red arrows indicate blood vessels. ***B***, The *k* values for mice before (black) and after ONC (blue). The black dashed lines track measurements for individual retinas before and after ONC. ***C***, ***D***, RGC axon bundle width distributions measured from the central (***C***) and the peripheral retina (***D***; NS: no significance; ****$p < 1e\text{-}4$); σ values indicate SDs.

capabilities to improve disease detection and management. Vis-OCT, combined with temporal speckle averaging (TSA), has also been used for visualizing RGC soma in WT rats, among other retinal cells (Pi et al., 2020), the IPL sublayers (Zhang et al., 2019b), and outer retina sublayers (Rubinoff et al., 2019). Using spectroscopic analysis, researchers applied vis-OCT to quantify retinal hemoglobin saturation in rodents (Yi et al., 2013; Chen et al., 2015b; Pi et al., 2020) and humans (Chen et al., 2017; Chong et al., 2017). Building on these demonstrated high-resolution and high-sensitivity imaging capabilities, we developed vis-OCTF to satisfy the need to map, quantify, and track the RGC axon bundle organization and damages throughout the entire fundus in mice following optic nerve injury. In future studies, we plan to develop and test vis-OCTF in human glaucoma patients. Several other groups, including us, have demonstrated the application of vis-OCT in humans (Chen et al., 2017; Song et al., 2018, 2020; Rubinoff et al., 2019; Zhang et al., 2019b), which is an essential first step in translating vis-OCTF from mouse to human subjects.

The acute ONC injury model was used in this study because it offers the advantage of examining neural degeneration in a relatively short time (two to four weeks; Puyang et al., 2016; Yi et al., 2016; Feng et al., 2017; Norat et al., 2021). As each crush surgery may produce varying degrees of optic nerve damage (Liu et al., 2020; Norat et al., 2021), it provides an ideal system to identify and track axon bundle changes *in vivo* in individuals. Figure 4*E* shows that the large bundles disappeared after ONC, which could be because of (1) one large bundle breaking down to two or more small ones, and/or (2) a bundle shrinking because of RGC loss. When bundles get smaller and the total bundle density does not change significantly, it is more likely because of the second scenario. Interestingly, we detected a 5% increase in RGC axon bundle layer thickness at 5 d after ONC (Fig. 5*H*), which has been reported in another study (Li et al., 2020). Such an increase in thickness could be caused by the initial inflammatory response induced by the ONC procedure, although the underlying mechanisms remain unclear (Mac Nair and Nickells, 2015; Williams et al., 2017).

The Sholl analysis results we obtained from ONC mice did not match our hypothesis in terms of statistical significance. This could be explained by the severity of ONC, low sample size, and/or variable image quality between subjects. To further explore the idea of using Sholl analysis to quantify RGC axon bundle network organization, we performed a simulation using the bundle width measurements we collected as input. We were able to simulate various possible bundle distributions for each condition investigated in this study. For each condition, the simulated and measured *k* values agreed well with each other. The simulation results demonstrate how the reduced bundle size after ONC leads to a higher *k*, suggesting a more rapid decrease in bundle density moving outward from the ONH. The simulation also explained how increased bundle size leads to a lower *k*, as with the $BAX^{-/-}$ mice. Overall, these findings from the simulation demonstrate the potential of Sholl analysis for characterizing the progression of RGC axon bundle damage.

One technical innovation in this study was introducing the circumpapillary B-scans with reduced speckle noise and increased sensitivity to track subtle changes in the retinal layer structure. However, the outcomes of this study were limited by manually performed measurements, missing portions of the montaged fibergram images, and optical defocus leading to measurement uncertainty. Impacts of manual measurement limitations were mitigated by closely following the measurement protocol described in Materials and Methods and reverifying outlier measurements. The impacts of the image quality limitations were reduced by excluding datasets with >10% missing

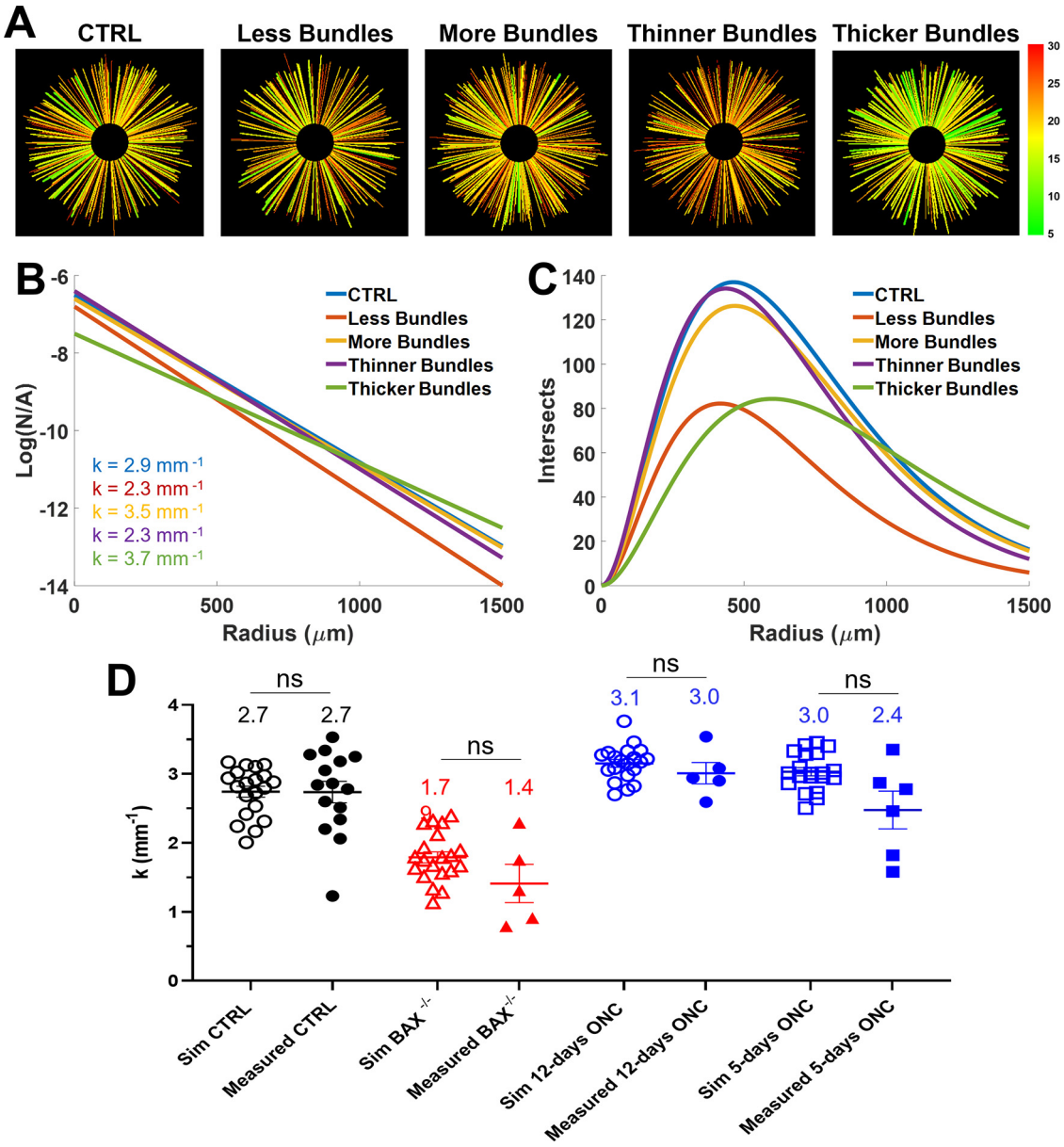

Figure 8. Model for simulating the relationship between the *k* value and the axon bundle width and number. ***A***, Simulated RGC axon bundle distributions. Simulated distributions include (from left to right): control (CTRL), low bundle density, high bundle density, thinner bundles, and thicker bundles. ***B***, Average semi-log *k* value for each simulated condition shown in panel ***A***. ***C***, Average number of simulated intersects for simulated conditions shown in panel ***A***. ***D***, Comparison between simulated *k* values (open shapes) and measured *k* values (filled shapes) for control (black), $BAX^{-/-}$ (red), and ONC (blue) mice. Simulations were performed based on the measured width of RGC axon bundles for each condition (NS: no significance).

area in the montaged fibergrams and datasets with low image quality. In the future, such limitations can be addressed by implementing new algorithms to automatically identify and measure the size parameters of individual bundles. Last, fibergram image quality can be improved using TSA (Zhang et al., 2019a; Pi et al., 2020).

Morphologic changes of RGCs with disease development and progression

Studies, including ours, suggested that changes in dendritic structure and synaptic functions of RGCs precede cell death in mice with experimental glaucoma (Puyang et al., 2015; Della Santina and Ou, 2017). Therefore, characterization of morphologic and functional degeneration of RGCs at early stages of glaucoma may open a time window for treatment to prevent subsequent vision loss. OCT has been increasingly applied to obtain objective measurements of the RNFL, ONH, macula, and GCIPL for assessing glaucoma progression for patients (Tatham and Medeiros, 2017; Schuman et al., 2020). However, two main concerns remain to be addressed: (1) whether the imaging technology offers high enough resolution and sensitivity to detect subtle changes in retinal substructure as discussed above, and (2) how the RGC morphologic changes are relevant to vision loss.

The GCIPL thickness has also been used as an indicator for glaucoma progression (Hou et al., 2013, 2018; Hammel et al., 2017). However, clinical studies reflect inconsistences between GCIPL and RNFL thickness changes and visual field (VF) progression with glaucoma development (Tatham and Medeiros, 2017; Schuman et al., 2020). For example, Hou and colleagues followed the RNFL and the GCIPL thinning and VF progression in 136 patients (231 eyes) with primary open-angle glaucoma for approximately six years (Hou et al., 2018). Approximately 25%

eyes showed progressive GCIPL thinning, 29% with RNFL thinning, and 15% showed both RNFL and GCIPL thinning, which were connected to an increased risk of VF progression. Seth and colleagues suggested that the structural change appears to be more useful in detection of progression in early disease states, whereas functional change is a better indicator as the disease progresses (Seth et al., 2018).

The changes in GCIPL thickness in mice could be because of changes in the RNFL, GCL, and/or the IPL. However, our current imaging system cannot separate individual layers clearly nor visualize sublayer changes (see the example in Fig. 1*B*). A thickening of the GCIPL was found in BAX$^{-/-}$ mice (Fig. 1*D*), which reflects the increased thickness of the RGC axon bundle layer, and possibly the increased IPL and/or GCL thickness (Fig. 1*E*). On the other hand, in the ONC model we observed a thinning of the GCIPL (Fig. 3*D*), coherently with the reduction of the RGC axon bundle layer thickness (Fig. 3*E*) and a thinner IPL following ONC injury. Future work is needed to visualize the sublayer structure of the IPL and the border of GCL/IPL. For example, TSA (Zhang et al., 2019a; Pi et al., 2020) could enhance image quality by visualization of RGC cellular structures and quantification of RGC soma loss associated with optic neuropathies in the living mouse retina.

Because individual RGCs respond differently to disease insult (Quigley et al., 1987; Troy and Shou, 2002; Feng et al., 2013; Chen et al., 2015a; Puyang et al., 2015), it is not surprising that the selective loss of a small number of RGCs and their dendritic trees may lead to a subtle change in the GCIPL thickness, especially at the early stages of glaucoma. For example, we showed that the dendritic branching of a subtype of ON cells, the SMI-32-positive ON cells, from the superior area of the retina was significantly reduced in the laser-photocoagulation-induced ocular hypertensive mice (Feng et al., 2013). By contrast, one subtype of the intrinsically photosensitive RGCs (ipRGCs), the M1 ipRGC, showed an increased dendritic field size at 7 and 60 d following the optic nerve transection (Pérez de Sevilla Müller et al., 2014). Moreover, the IPL can be divided into the ON and the OFF sublayers. The changes in the ON and OFF pathways may also contribute to the differences in the sublayer structural changes. Della Santina and colleagues showed that OFF-transient RGCs exhibited decreased dendritic length and number of dendrites at two to four weeks post IOP elevation (Della Santina and Ou, 2017). At six to eight weeks after IOP elevation, our studies showed that the dendritic coverage of mono-laminated ON cells decreased (Feng et al., 2013). A better visualization and tracking of changes in the sublayer structure in glaucomatous mice could present a fundamental advancement in glaucoma diagnosis and management.

RGC axon bundle morphology as a novel indicator for RGC health

Every RGC extends one single axon projecting to higher visual centers in the brain. In humans, the total number of RGCs varies from 0.7 to 1.5 million (Curcio and Allen, 1990). Within each retina, the spatial distribution of RGCs is not even, e.g., densities in the nasal region are three times higher than the temporal region in the peripheral area of human retinas (Curcio and Allen, 1990). Similarly, the total number and spatial distribution of RGCs also vary in mice and monkeys (Spear et al., 1996; Jeon et al., 1998). In other words, individuals may develop a unique axon bundle density and organization; thus, characterization of RGC axon bundle structure could offer an accurate and unique reference point for tracking RGC changes for individuals with disease development.

It is also largely unknown whether and how RGC axon bundles change in response to different disease insults. For example, RGC axons fasciculate using cell adhesion molecules such as Down syndrome cell adhesion molecule (DSCAM), which promotes fasciculation of axons in the developing mouse optic pathway through homotypic interactions (Erskine and Herrera, 2007; Yamagata and Sanes, 2008; Bruce et al., 2017). In rats injected with hypertonic saline to induce glaucoma-like conditions, defasciculation of axon strands off the main axon fascicles was observed, and prevention of axon bundle defasciculation reduced RGC loss with glaucoma development (Mata et al., 2015). Within individual axons, the cytoskeletal structure, including microtubules and F-actin filaments, shows signs of distortion at the early stages of ocular hypertension, which may contribute to changes in RNFL optical properties (Huang and Knighton, 2005; Huang et al., 2017). Combining vis-OCT imaging and genetic tools to manipulate molecules involved in bundle formation and breakdown, we may start to understand how axon bundles change with RGC degeneration and death in diseased conditions.

References

Anton A, Zangwill L, Emdadi A, Weinreb RN (1997) Nerve fiber layer measurements with scanning laser polarimetry in ocular hypertension. Arch Ophthalmol 115:331–334.

Bruce FM, Brown S, Smith JN, Fuerst PG, Erskine L (2017) DSCAM promotes axon fasciculation and growth in the developing optic pathway. Proc Natl Acad Sci USA 114:1702–1707.

Cang J, Savier E, Barchini J, Liu X (2018) Visual function, organization, and development of the mouse superior colliculus. Annu Rev Vis Sci 4:239–262.

Chen H, Zhao Y, Liu M, Feng L, Puyang Z, Yi J, Liang P, Zhang HF, Cang J, Troy JB, Liu X (2015a) Progressive degeneration of retinal and superior collicular functions in mice with sustained ocular hypertension. Invest Ophthalmol Vis Sci 56:1971–1984.

Chen S, Yi J, Zhang HF (2015b) Measuring oxygen saturation in retinal and choroidal circulations in rats using visible light optical coherence tomography angiography. Biomed Opt Express 6:2840–2853.

Chen S, Shu X, Nesper PL, Liu W, Fawzi AA, Zhang HF (2017) Retinal oximetry in humans using visible-light optical coherence tomography. Biomed Opt Express 8:1415–1429.

Chong SP, Bernucci M, Radhakrishnan H, Srinivasan VJ (2017) Structural and functional human retinal imaging with a fiber-based visible light OCT ophthalmoscope. Biomed Opt Express 8:323–337.

Chong SP, Zhang T, Kho A, Bernucci MT, Dubra A, Srinivasan VJ (2018) Ultrahigh resolution retinal imaging by visible light OCT with longitudinal achromatization. Biomed Opt Express 9:1477–1491.

Curcio CA, Allen KA (1990) Topography of ganglion cells in human retina. J Comp Neurol 300:5–25.

Da Pozzo S, Marchesan R, Ravalico G (2009) Scanning laser polarimetry - a review. Clin Exp Ophthalmol 37:68–80.

Della Santina L, Ou Y (2017) Who's lost first? Susceptibility of retinal ganglion cell types in experimental glaucoma. exp. Eye Res 158:43–50.

Donato A, Kagias K, Zhang Y, Hilliard MA (2019) Neuronal sub-compartmentalization: a strategy to optimize neuronal function. Biol Rev Camb Philos Soc 94:1023–1037.

Dong ZM, Wollstein G, Wang B, Schuman JS (2017) Adaptive optics optical coherence tomography in glaucoma. Prog Retin Eye Res 57:76–88.

Erskine L, Herrera E (2007) The retinal ganglion cell axon's journey: insights into molecular mechanisms of axon guidance. Dev Biol 308:1–14.

Feng L, Zhao Y, Yoshida M, Chen H, Yang JF, Kim TS, Cang J, Troy JB, Liu X (2013) Sustained ocular hypertension induces dendritic degeneration

of mouse retinal ganglion cells that depends on cell type and location. Invest Ophthalmol Vis Sci 54:1106–1117.

Feng L, Puyang Z, Chen H, Liang P, Troy JB, Liu X (2017) Overexpression of brain-derived neurotrophic factor protects large retinal ganglion cells after optic nerve crush in mice. eNeuro 4: ENEURO.0331-16.2016.

Hammel N, Belghith A, Weinreb RN, Medeiros FA, Mendoza N, Zangwill LM (2017) Comparing the rates of retinal nerve fiber layer and ganglion cell-inner plexiform layer loss in healthy eyes and in glaucoma eyes. Am J Ophthalmol 178:38–50.

Hood DC (2017) Improving our understanding, and detection, of glaucomatous damage: an approach based upon optical coherence tomography (OCT). Prog Retin Eye Res 57:46–75.

Hou HW, Lin C, Leung CK (2013) Integrating macular ganglion cell inner plexiform layer and parapapillary retinal nerve fiber layer measurements to detect glaucoma progression. Ophthalmology 120:2485–2492.

Hou HW, Lin C, Leung CK (2018) Integrating macular ganglion cell inner plexiform layer and parapapillary retinal nerve fiber layer measurements to detect glaucoma progression. Ophthalmology 125:822–831.

Huang XR, Knighton RW (2005) Microtubules contribute to the birefringence of the retinal nerve fiber layer. Invest Ophthalmol Vis Sci 46:4588–4593.

Huang XR, Knighton RW, Spector YZ, Qiao J, Kong W, Zhao Q (2017) Reflectance spectrum and birefringence of the retinal nerve fiber layer with hypertensive damage of axonal cytoskeleton. Invest Ophthalmol Vis Sci 58:2118–2129.

Jeon CJ, Strettoi E, Masland RH (1998) The major cell populations of the mouse retina. J Neurosci 18:8936–8946.

Jonas JB, Aung T, Bourne RR, Bron AM, Ritch R, Panda-Jonas S (2017) Glaucoma. Lancet 390:2183–2193.

Kerrigan-Baumrind LA, Quigley HF, Pease ME, Kerrigan DF, Mitchell RS (2000) Number of ganglion cells in glaucoma eyes compared with threshold visual field tests in the same persons. Invest Ophthalmol Vis Sci 41:741–748.

Li L, Huang H, Fang F, Liu L, Sun Y, Hu Y (2020) Longitudinal morphological and functional assessment of RGC neurodegeneration after optic nerve crush in mouse. Front Cell Neurosci 14:109.

Libby RT, Li Y, Savinova OV, Barter J, Smith RS, Nickells RW, John SW (2005) Susceptibility to neurodegeneration in a glaucoma is modified by Bax gene dosage. PLoS Genet 1:17–26.

Liu X, Feng L, Shinde I, Cole JD, Troy JB, Saggere L (2020) Correlation between retinal ganglion cell loss and nerve crush force-impulse established with instrumented tweezers in mice. Neurol Res 42:379–386.

Mac Nair CE, Nickells RW (2015) Neuroinflammation in glaucoma and optic nerve damage. Prog Mol Biol Transl Sci 134:343–363.

Maes ME, Schlamp CL, Nickells RW (2017) BAX to basics: how the BCL2 gene family controls the death of retinal ganglion cells. Prog Retin Eye Res 57:1–25.

Mata D, Linn DM, Linn CL (2015) Retinal ganglion cell neuroprotection induced by activation of alpha7 nicotinic acetylcholine receptors. Neuropharmacology 99:337–346.

Miller DA, Grannonico M, Liu M, Kuranov RV, Netland PA, Liu X, Zhang HF (2020) Visible-light optical coherence tomography fibergraphy for quantitative imaging of retinal ganglion cell axon bundles. Transl Vis Sci Technol 9:11.

Norat P, Gao J, Soldozy S, Zhang HF, Liu X (2021) A standardized crush tool to produce consistent retinal ganglion cell damage in mice. Neural Regen Res 16:1442–1443.

Pérez de Sevilla Müller L, Sargoy A, Rodriguez AR, Brecha NC (2014) Melanopsin ganglion cells are the most resistant retinal ganglion cell type to axonal injury in the rat retina. PLoS One 9:e93274.

Pi S, Hormel TT, Wei X, Cepurna W, Morrison JC, Jia Y (2020) Imaging retinal structures at cellular-level resolution by visible-light optical coherence tomography. Opt Lett 45:2107–2110.

Puyang Z, Chen H, Liu X (2015) Subtype-dependent morphological and functional degeneration of retinal ganglion cells in mouse models of experimental glaucoma. J Nat Sci 1:e103.

Puyang Z, Feng L, Chen H, Liang P, Troy JB, Liu X (2016) Retinal ganglion cell loss is delayed following optic nerve crush in NLRP3 knockout mice. Sci Rep 6:20998.

Quigley HA (2011) Glaucoma. Lancet 377:1367–1377.

Quigley HF, Sanchez RM, Dunkelberger GR, L'Hernault NL, Baginski TA (1987) Chronic glaucoma selectively damages large optic nerve fibers. Invest Ophthalmol Vis Sci 28:913–920.

Rangarajan KV, Lawhn-Heath C, Feng L, S KT, Cang J, Liu X (2011) Detection of visual deficits in aging DBA/2J mice by two behavioral assays. Curr Eye Res 36:481–491.

Rovere G, Nadal-Nicolás FM, Agudo-Barriuso M, Sobrado-Calvo P, Nieto-López L, Nucci C, Villegas-Pérez MP, Vidal-Sanz M (2015) Comparison of retinal nerve fiber layer thinning and retinal ganglion cell loss after optic nerve transection in adult albino rats. Invest Ophthalmol Vis Sci 56:4487–4498.

Rubinoff I, Beckmann L, Wang Y, Fawzi AA, Liu X, Tauber J, Jones K, Ishikawa H, Schuman JS, Kuranov R, Zhang HF (2019) Speckle reduction in visible-light optical coherence tomography using scan modulation. Neurophotonics 6:041107.

Schuman JS, Kostanyan T, Bussel I (2020) Review of longitudinal glaucoma progression: 5 years after the Shaffer lecture. Ophthalmol Glaucoma 3:158–166.

Sernagor E, Eglen SJ, Wong RO (2001) Development of retinal ganglion cell structure and function. Prog Retin Eye Res 20:139–174.

Seth NG, Kaushik S, Kaur S, Raj S, Pandav SS (2018) 5-year disease progression of patients across the glaucoma spectrum assessed by structural and functional tools. Br J Ophthalmol 102:802–807.

Shu X, Beckmann L, Zhang H (2017) Visible-light optical coherence tomography: a review. J Biomed Opt 22:1–14.

Shu X, Beckmann L, Wang Y, Rubinoff I, Lucy K, Ishikawa H, Wollstein G, Fawzi AA, Schuman JS, Kuranov RV, Zhang HF (2019) Designing visible-light optical coherence tomography towards clinics. Quant Imaging Med Surg 9:769–781.

Soetikno BT, Beckmann L, Zhang X, Fawzi AA, Zhang HF (2018) Visible-light optical coherence tomography oximetry based on circumpapillary scan and graph-search segmentation. Biomed Opt Express 9:3640–3652.

Song W, Zhou L, Zhang S, Ness S, Desai M, Yi J (2018) Fiber-based visible and near infrared optical coherence tomography (vnOCT) enables quantitative elastic light scattering spectroscopy in human retina. Biomed Opt Express 9:3464–3480.

Song W, Shao W, Yi W, Liu R, Desai M, Ness S, Yi J (2020) Visible light optical coherence tomography angiography (vis-OCTA) facilitates local microvascular oximetry in the human retina. Biomed Opt Express 11:4037–4051.

Spear PD, Kim CB, Ahmad A, Tom BW (1996) Relationship between numbers of retinal ganglion cells and lateral geniculate neurons in the rhesus monkey. Vis Neurosci 13:199–203.

Stein DM, Ishikawa H, Hariprasad R, Wollstein G, Noecker RJ, Fujimoto JG, Schuman JS (2006) A new quality assessment parameter for optical coherence tomography. Br J Ophthalmol 90:186–190.

Syc-Mazurek SB, Libby RT (2019) Axon injury signaling and compartmentalized injury response in glaucoma. Prog Retin Eye Res 73:100769.

Tatham AJ, Medeiros FA (2017) Detecting structural progression in glaucoma with optical coherence tomography. Ophthalmology 124:S57–S65.

Templeton JP, Geisert EE (2012) A practical approach to optic nerve crush in the mouse. Mol Vis 18:2147–2152.

Thomson BR, Grannonico M, Liu F, Liu M, Mendapara P, Xu Y, Liu X, Quaggin SE (2020) Angiopoietin-1 knockout mice as a genetic model of open-angle glaucoma. Transl Vis Sci Technol 9:16.

Tran NM, Shekhar K, Whitney IE, Jacobi A, Benhar I, Hong G, Yan W, Adiconis X, Arnold ME, Lee JM, Levin JZ, Lin D, Wang C, Lieber CM, Regev A, He Z, Sanes JR (2019) Single-cell profiles of retinal ganglion cells differing in resilience to injury reveal neuroprotective genes. Neuron 104:1039–1055.

Troy JB, Shou T (2002) The receptive fields of cat retinal ganglion cells in physiological and pathological states: where we are after half a century of research. Prog Retin Eye Res 21:263–302.

Whitmore AV, Libby RT, John SW (2005) Glaucoma: thinking in new ways-a rôle for autonomous axonal self-destruction and other compartmentalised processes? Prog Retin Eye Res 24:639–662.

Williams PA, Marsh-Armstrong N, Howell GR; Lasker/IRRF Initiative on Astrocytes and Glaucomatous Neurodegeneration Participants (2017) Neuroinflammation in glaucoma: a new opportunity. Exp Eye Res 157:20–27.

Wollstein G, Garway-Heath DF, Hitchings RA (1998) Identification of early glaucoma cases with the scanning laser ophthalmoscope. Ophthalmology 105:1557–1563.

Wollstein G, Garway-Heath DF, Fontana L, Hitchings RA (2000) Identifying early glaucomatous changes. Comparison between expert clinical assessment of optic disc photographs and confocal scanning ophthalmoscopy. Ophthalmology 107:2272–2277.

Yamagata M, Sanes JR (2008) DSCAM and Sidekick proteins direct lamina-specific synaptic connections in vertebrate retina. Nature 451:465–469.

Yi J, Wei Q, Liu W, Backman V, Zhang HF (2013) Visible-light optical coherence tomography for retinal oximetry. Opt Lett 38:1796–1798.

Yi J, Chen S, Shu X, Fawzi AA, Zhang HF (2015) Human retinal imaging using visible-light optical coherence tomography guided by scanning laser ophthalmoscopy. Biomed Opt Express 6:3701–3713.

Yi J, Puyang Z, Feng L, Duan L, Liang P, Backman V, Liu X, Zhang HF (2016) Optical detection of early damage in retinal ganglion cells in a mouse model of partial optic nerve crush injury. Invest Ophthalmol Vis Sci 57:5665–5671.

Zhang P, Miller EB, Manna SK, Meleppat RK, Pugh EN Jr, Zawadzki RJ (2019a) Temporal speckle-averaging of optical coherence tomography volumes for in-vivo cellular resolution neuronal and vascular retinal imaging. Neurophotonics 6:041105.

Zhang T, Kho AM, Srinivasan VJ (2019b) Improving visible light OCT of the human retina with rapid spectral shaping and axial tracking. Biomed Opt Express 10:2918–2931.